Mechanical Systems and Signal Processing 165 (2022) 108339

Contents lists available at ScienceDirect

Mechanical Systems and Signal Processing

journal homepage: www.elsevier.com/locate/ymssp

A unified equivalent circuit and impedance analysis method for galloping piezoelectric energy harvesters

Chunbo Lan [a], Yabin Liao [b,*], Guobiao Hu [c]

[a] *College of Aerospace Engineering, Nanjing University of Aeronautics and Astronautics, Nanjing, PR China*
[b] *Department of Aerospace Engineering, Embry-Riddle Aeronautical University–Prescott, Prescott, AZ, USA*
[c] *School of Civil and Environmental Engineering, Nanyang Technological University, 50 Nanyang Avenue, 639798, Singapore*

ARTICLE INFO

Keywords:
Galloping
Piezoelectric
Energy harvesting
Equivalent circuit
Impedance
Electromechanical coupling

ABSTRACT

In the past decade, galloping-based energy harvesters (GPEH) connected with various interface circuits have been developed and analytical models have been built. However, the power performances of these advanced structures and circuits are always treated separately, and a general model is missing to gain insights at a system level. To tackle this issue, this paper proposes a unified analysis framework for GPEHs. Its results are consistent with validated (but disconnected) results in the literature. The method provides an integrated view of the physics of linear GPEHs in multiple domains at the system level, and elucidates the similarities and differences among power behaviors of GPEHs connected with various interface circuits. The framework is based on two major elements: an equivalent circuit that represents the entire system, and an equivalent impedance that represents the interface circuit. Firstly, the electromechanical system is linearized and modeled in the electrical domain by an equivalent self-excited circuit with a negative resistive element representing the external aerodynamic excitation, and a general load impedance representing the interface circuit. Then, a closed-form, analytical expression of the harvested power is obtained based on the Kirchhoff's Voltage Law, from which the optimal load, maximum power, power limit, and critical electromechanical coupling (minimum coupling to reach the power limit) are determined. In this unified analysis, the exact type of energy harvesting interface circuit is not assumed. After that, the power characteristics of a GPEH connected with five representative interface circuits are analytically derived and discussed, by using the particular equivalent impedance of the interface circuit of interest. It is shown that they are subjected to the same power limit. However, the critical electromechanical coupling depends on the type of circuit. Throughout the discussions, impedance plots are used to illustrate the relationship between the internal system characteristics and external load impedance, facilitating the understanding of system power behavior.

1. Introduction

In the past few decades, low-power-consumption microelectronics, such as wireless sensors, wearable electronics and internet of things have been rapidly developed. To supply reliable energy to these low-power-consumption micro devices, energy harvesting technology has been increasingly advanced by many researchers to harness the green energy, such as solar, heat, vibration, and wind in

---

* Corresponding author.
E-mail address: Yabin.Liao@erau.edu (Y. Liao).

https://doi.org/10.1016/j.ymssp.2021.108339
Received 10 June 2021; Received in revised form 3 August 2021; Accepted 8 August 2021

our environment [1]. In the area of small-scale wind energy harvesting, aeroelastic energy harvesting has become one of the most promising technologies [2]. Recently, several flow-induced-vibration mechanisms [3–10], such as vortex-induced vibration [3–5], flutter [6,7], galloping [8,9], and wake galloping [10,11], have been introduced into aeroelastic energy harvesting. Among these mechanisms, the galloping-based energy harvester has high energy harvesting efficiency as a result of the large structural response during the induced limit cycle oscillation when galloping takes place, leading to a large output power [8,9].

To improve the performance of galloping energy harvesting, researchers have devoted most of the efforts to two important aspects in the past few decades [2,12]: structural design [13–33], and energy harvesting interface circuit design [34–39]. In the structural design aspect, the bluff body and piezoelectric beams are the main design focuses. The feasibility of galloping energy harvesting was theoretically demonstrated by Barrero-Gil et al. [8] and experimentally validated by Sirohi et al. [13,14]. In Sirohi's experiment, a bluff body was designed as D-shaped cross section, and results showed that the power output increased rapidly with the increase of the wind speed when galloping occurred. To improve the output power, the geometry of the bluff body was then designed as a square section [15], a triangle section [16], etc. Yang et al. [17] studied the influence of the cross-section geometry on the performance of a galloping piezoelectric energy harvester. They found that the performance of square cross-section geometry was better than that of the triangles, D-section and rectangle geometries. Recently, Wang et al. investigated a GPEH with isosceles triangular cross-section bluff bodies with different vortex angles [18] and proposed a butterfly-shaped bluff body to improve the efficiency of low-speed wind energy harvesting [19]. Sun et al. [20] proposed a nested bluff-body structure and experimental results indicated a significant power density increase of 27.8%. Sun et al. [21] proposed a bulb cross-sectional cylinder to maximize the output power of coupled vortex-induced vibration and galloping phenomenon. More recently, the concept of metasurface was introduced by Wang et al. [22] into the bluff body design to enhance vortex induced energy harvesting and machine learning method was used by Zhang et al. [23] to predict the response of wind energy harvesters. Meanwhile, nonlinear GPEH and multi-degree-of-freedom GPEH have received growing interests in recent years. Bibo et al. [24,25] proposed a nonlinear galloping energy harvester by introducing the nonlinear restoring force. It was revealed that the inter-well oscillation of the bistable configuration outperformed the high-energy oscillation of the monostable configuration. Such a nonlinear restoring force was also utilized in the wake of galloping energy harvesting by Alhadidi et al. [26] to largely broaden the bandwidth. Wang et al. [27] furtherly developed a tristable GPEH. Their experimental results showed that the maximum power reached 0.73 mW at 7.0 m/s wind speed. Zhao et al. [28] recently proposed an impact-based energy harvester, which integrated the conventional GPEH with an elastic stopper to achieve broadband energy harvesting. Besides, Lan et al. [29] developed a two-degree-of-freedom (2-DOF) GPEH from the conventional single-degree-of-freedom (SDOF) GPEH. It is found that the cut-in wind speed of 2-DOF GPEH is closely related to the mass, stiffness, and damping, which makes it possible to efficiently tune the cut-in wind speed of GPEH by tuning the mass or stiffness of mechanical structures. This analytical prediction was experimentally validated by Hu et al. [30]. Zhao et al. [31] proposed a nonlinear 2-DOF GPEH consisting of a cut-out cantilever and several magnets. Their experiments showed that the cut-in wind speed was largely decreased owing to the introduction of nonlinearity. Yang et al. [32] developed a magnetically coupled dual-beam GPEH and experimentally observed that the cut-in wind speed can be reduced up to 41.9%. They [33] furtherly conducted a stochastic analysis on a galloping energy harvesting since the wind speed is random on a buoy platform.

In the aspect of interface circuit design, various interface circuits, such as AC, AC/DC, synchronized charge extraction (SCE), switch harvesting on inductor (SSHI) circuits, are employed in GEPH. Abdelmoula et al. [34] studied the effect of electrical impedance on the performance of galloping-based energy harvester. Tan et al. [35] studied the optimal performance of the conventional GPEH with a pure resistance based on the analytical solution. Zhao et al. [36] studied the performance of a GPEH with a SSHI power conditioning circuit. It was found that with a weak-coupling harvester operating at a wind speed of 7 m/s, the SSHI could harvest up to 143% more wind power than the standard circuit. Then, Zhao et al. [37] derived the analytical solutions of a conventional GPEH with standard rectified AC/DC, SCE, and SSHI circuits. A comprehensive comparison of these four electrical interfacing circuits in the conventional GPEH was conducted by Zhao et al. [38], and the advantages and disadvantages of these four circuits were discussed. Recently, Wang et al. [39] studied the performance of a tapered beam based GPEH with four direct-current circuits by using finite element methods, Simulink simulations, and wind tunnel experiments.

It is important to note that in the aforementioned investigations, usually, the structure design and circuit design were focused separately. In the structure design studies [13–33], the interface circuit is most likely to be a pure resistance. In the interface circuit design studies [34–39], the structure is usually a classical piezoelectric cantilever beam with a common bluff body. As a result, although a lot of novel structures and advanced circuits have been developed separately in the past few years, the performance of a novel GPEH with advanced structure and circuit design is still an open question to be explored. A similar phenomenon can be found in the research of vibration energy harvesting [40–41]. Two important methods have been applied in vibration energy harvesting to overcome this issue and build a bridge between the structural and circuitry aspects. The first one is the equivalent circuit method [40], which uses equivalent electrical elements to represent the mechanical components so that the entire electromechanical system is represented and analyzed in the same electrical domain. As a result, the dynamic responses of novel piezoelectric structures with advanced interface circuits can be simulated and studied by using circuit simulation and analysis methods. The second one is the impedance matching method [41]. The system impedances can be categorized into two groups: mechanical (or source) impedance and electrical (or load) impedance. Maximum power is obtained when these two impedances satisfy the impedance matching condition. The impedance matching method has been widely used in vibration energy harvesting studies since it makes the power analysis more convenient and efficient than conventional analytical methods. Based on these two methods, the analytical study and numerical simulation of novel vibration energy harvesters with advanced interfaces can be performed [42–45]. For this reason, it is quite promising to leverage these useful methods into galloping energy harvesting to solve similar problems.

Recently, the equivalent circuit method is introduced by Tang et al. [46] for numerical studies of galloping energy harvester. They used the equivalent circuit method to simulate the dynamic responses of the linear GPEH with various interface circuits, such as SCE circuit and SSHI circuits. In these studies [37–38,46], the numerical results predicted by the equivalent circuit method agreed very well with the analytical solutions and experimental results. However, the analytical solutions in their works were derived from the governing electromechanically coupled equations by using the harmonic balance method, and the equivalent circuit was used for numerical simulation. In addition, in the studies, each type of the interface circuits was treated separately. As a result, though the results for various interface circuits shared similarities along with differences, a deeper understanding of these similarities and differences is difficult.

This paper is motivated to make several new contributions to the analytical modeling and analysis of GPEHs. The first and the most important contribution is that a general model is developed to unify GPEHs connected with various types of interface circuits. The unified model is based on the power expression for a linear GPEH connected with a generic load impedance representing the effect of the interface circuit. As a result, the model provides insights into the similarities in the system behavior of GPEHs connected with different interface circuits. On the other hand, for a specific type of interface circuit, the load impedance assumes a particular form, i.e., equivalent impedance. This leads to differences in their associated system behavior. The concept of equivalent impedance of interface circuits has been successfully applied by Liao and Liang [43] to obtain a unified model of vibration-based PEHs (VPEH) that offers excellent insights on their system behaviors. However, it has not been attempted on GPEHs, which have different underlying physics from that of VPEHs. It will be shown that the approach to obtain the unified model of GPEHs is similar (both use the equivalent impedance concept) but also different from that for VPEHs to adapt to the unique physics. The second contribution is that we propose a new equivalent circuit that models the external aerodynamic excitation through a negative resistive element. The circuit is self-excited without an explicit voltage or current source, as in the case of VPEHs. As a result, the conventional impedance matching method is not suitable. Applying circuit laws to the equivalent circuit with a general electrical (load) impedance yields the analytical expression of the harvested power, which is the foundation of the unified model. Though the concept of equivalent circuit is not new and it has been applied to GPEHs in the literature (e.g., [36–38,46]), the idea of modeling the aerodynamic interaction and excitation through a negative-resistance element and consequently representing the system as a self-excited circuit is novel. This new equivalent circuit allows for the derivation of the power expression of the unified model conveniently. Note that the approach of using negative resistance to achieve self-excitation was physically implemented by Lan et al. [47] on nonlinear vibration-based PEHs, resulting in high-energy responses triggered by voltage impulse perturbations. Here, we use an equivalent negative resistance to theoretically model the intrinsic, self-excitation physics of galloping-based PEHs. The third important contribution of the paper is the analytical expression of a GPEH's power limit (the maximum possible harvested power through the tuning of the interface circuit regardless of the type of the interface circuit) along with the minimum required electromechanical coupling to reach the power limit. It is important to note that while the conventional impedance matching method has been successfully used [43,44] to obtain the power limit of VPEHs, it cannot be applied to GPEHs here. In a conventional impedance matching configuration, there is a fixed voltage or current source, e.g., representing the vibration excitation in the case of VPEHs, and the load impedance is tuned to match the source impedance. However, since the excitation physics are represented by resistive elements for GPEHs, there is not an equivalent voltage or current source. Instead, we will apply circuit laws to determine the harvested power in general, and then obtain the power limit along its conditions. The final important contribution is that many of the relationships and discussions are illustrated graphically by impedance plots, facilitating the understanding of important concepts visually.

It is important to point out that the main aim of this paper is to present a general methodology for modeling and analyzing GPEHs, which elucidates the underlying coupled dynamics of the system. While some of the results are not new, the proposed method offers a new and unified view of the results that have scattered in the literature. In fact, the agreement between the results in this paper and those previously obtained and validated by other researchers [37] serves as a validation of the proposed method and model. Note that since the methodology is general, its application is not limited to only those selected interface circuits in Section 4. It can be extended to other interface circuits as well.

The main contents of this paper are organized as follows: Section 2 describes the system modeling and new equivalent circuit of GPEHs. Section 3 presents the detailed derivation of the unified model of GPEH. Section 4 uses the unified model to analytically study the power performance of GPEHs with different interface circuits, and also presents a comprehensive comparison. Finally, the main conclusions are summarized in Section 5.

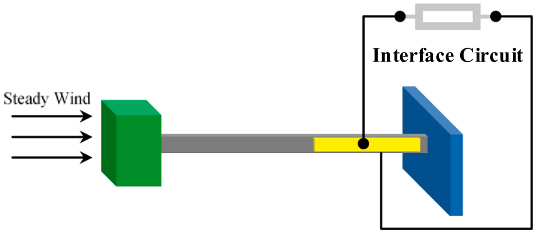

Fig. 1. Configuration of a typical GPEH system.

2. System modeling and equivalent circuit

2.1. System modeling

A typical GPEH, as shown in Fig. 1, consists of a piezoelectric cantilever beam with a bluff body mounted at its free end. The effect of wind flow on the mechanical structure can be represented by an aerodynamic force. When the wind speed increases to a certain level, the aerodynamic force is large enough to cause the mechanical system to lose its stability and attain a large structural oscillation, i.e., galloping motion. When galloping takes place, the piezoelectric transducer experiences large deformation and generates an electric output voltage. Hence, the wind energy is harvested and transformed into electrical energy.

Based on the assumption of linear electromechanical coupling and elasticity behaviours, a lumped SDOF GPEH model commonly used in the literature [18–21,48] is governed by the following electromechanically-coupled equations:

$$\begin{cases} M\ddot{x}(t)+C\dot{x}(t)+Kx(t)-\theta v_p(t)=F_a \\ \quad \theta\dot{x}(t)\ +\ C_p\dot{v}_p(t)+\dot{q}(t)=0 \end{cases}, \tag{1}$$

where M, C, and K, are the effective mass, damping, and stiffness of the SDOF GPEH, respectively. The effective damping can be expressed as $C=2\zeta\omega_n M$, where ζ is the damping ratio and ω_n is the natural frequency; θ is the electromechanical coupling coefficient; C_p is the clamped capacitance of the piezoelectric transducer; x is the displacement relative to the base; v_p is the voltage across the piezoelectric element (also the external energy harvesting interface circuit); q is the electric charge; and F_a is the vertical component of the aerodynamic force acting on the bluff body.

To represent the aerodynamic force, the quasi-steady assumption is widely used in galloping energy harvesting. In the quasi-steady assumption [48], the motion of the bluff body is assumed to be very slow compared to the motion of wind. Under this assumption, the coefficients of aerodynamic force stay constant for a given angle of attack. According to Barrero-Gil [8], the aerodynamic force F_a can be modelled as

$$F_a=\frac{1}{2}\rho LDU^2\left[s_1\frac{\dot{x}}{U}-s_3\left(\frac{\dot{x}}{U}\right)^3\right], \tag{2}$$

where L and D are the crossflow length and width of the bluff body, respectively. ρ and U are the air density and wind speed, respectively. And s_1 and s_3 are the empirical linear and cubic coefficients of the transverse galloping force, which are dependent on the cross-section geometry of the prismatic structure. Submitting Eq. (2) into Eq. (1), the governing equations of a SDOF GPEH are rewritten as

$$\begin{cases} M\ddot{x}+C\dot{x}\ +\ Kx-\theta v_p=\frac{1}{2}\rho ULD\left[s_1\dot{x}-\frac{s_3}{U^2}(\dot{x})^3\right] \\ \qquad \theta\dot{x}(t)\ +\ C_p\dot{v}_p(t)+\dot{q}(t)=0 \end{cases} \tag{3}$$

2.2. Equivalent circuit

This paper aims to develop a unified model to analyze the power characteristics of galloping PEHs interfaced with various energy harvesting circuits, and provide perspectives on the system behavior in a systematic matter. For this purpose, the equivalent circuit representation has been shown to be an effective approach [46]. The coupled-field physics of the system can be entirely represented in the electrical domain, where the effect and dynamics of energy harvesting interface circuits can be analyzed conveniently in one domain. To derive the equivalent circuit, the aerodynamic force expression in Eq. (3) needs to be rewritten in a "linear" form. The harmonic-balance linearization method, which has been successfully used in the impedance matching analysis of a monostable piezoelectric energy harvester [42], can be applied here for this purpose. In the harmonic balance method, the solution of Eq. (3) is assumed to be

$$\begin{cases} x=a\sin(\omega t)+b\cos(\omega t) \\ \dot{x}=a\omega\cos(\omega t)-b\omega\sin(\omega t) \end{cases}, \tag{4}$$

where ω is the vibration frequency of the system, and a and b are the structural response constants. Submitting Eq. (4) into the cubic term of the first part of Eq. (3) and neglecting high order harmonics, we have

$$\begin{aligned} \dot{x}^3&=[a\omega\cos(\omega t)-b\omega\sin(\omega t)]^3 \\ &\approx\omega^3\left[\frac{3}{4}a^3\cos(\omega t)+\frac{3}{4}ab^2\cos(\omega t)-\frac{3}{4}a^2b\sin(\omega t)-\frac{3}{4}b^3\sin(\omega t)\right], \\ &=\frac{3}{4}r^2\omega^2\dot{x} \end{aligned} \tag{5}$$

where r is the amplitude of the structural response, i.e.,

$$r^2 = a^2 + b^2. \tag{6}$$

Substituting expression (5) into Eq. (2) yields the equivalent aerodynamic force

$$F_a = \frac{1}{2}\rho LDU\left(s_1 - \frac{3r^2\omega^2 s_3}{4U^2}\right)\dot{x}, \tag{7}$$

which can then be substituted into the governing equation (3) to yield the approximately equivalent equations:

$$\begin{cases} M\ddot{x}(t) + \left[C - \frac{1}{2}\rho LDU\left(s_1 - \frac{3r^2\omega^2 s_3}{4U^2}\right)\right]\dot{x}(t) + Kx(t) - \theta v_p(t) = 0 \\ \theta\dot{x}(t) \ + \ C_p\dot{v}_p(t) + \dot{q}(t) = 0 \end{cases} \tag{8}$$

To derive the voltage relationship of the equivalent circuit, rewrite the first equation of (8) as

$$\frac{M}{\theta^2}\frac{d}{dt}[-\theta\dot{x}(t)] + \frac{1}{\theta^2}\left[C - \frac{1}{2}\rho LDU\left(s_1 - \frac{3r^2\omega^2 s_3}{4U^2}\right)\right][-\theta\dot{x}(t)] + \frac{K}{\theta^2}\int[-\theta\dot{x}(t)]dt + v_p(t) = 0. \tag{9}$$

Define the equivalent current

$$i_{eq} = -\theta\dot{x}(t) \tag{10}$$

and rewrite Eq. (9) as

$$\frac{M}{\theta^2}\frac{di_{eq}}{dt} + \frac{C}{\theta^2}i_{eq} - \frac{\rho LDUs_1}{2\theta^2}i_{eq} + \frac{3\rho LDs_3r^2\omega^2}{8U\theta^2}i_{eq} + \frac{K}{\theta^2}\int i_{eq}dt + v_p(t) = 0. \tag{11}$$

This can be rewritten further as an equivalent voltage relationship in a closed-loop circuit

$$L_s\frac{di_{eq}}{dt} + R_s i_{eq} + R_1 i_{eq} + R_3 i_{eq} + \frac{\int i_{eq}dt}{C_s} + v_p(t) = 0, \tag{12}$$

where the first five terms on the left represent the voltage drops over an equivalent inductor, three resistors, and a capacitor, respectively. The last term, v_p is the voltage across the external energy harvesting circuit. By comparing Eqs. (11) and (12), the equivalent electrical elements are defined as

$$L_s = \frac{M}{\theta^2}, R_s = \frac{C}{\theta^2}, R_1 = -\frac{\rho LDUs_1}{2\theta^2}, R_3 = \frac{3\rho LDs_3r^2\omega^2}{8U\theta^2}, C_s = \frac{\theta^2}{K}, \tag{13}$$

where L_s, R_s, C_s represent the mass, damping, and stiffness of the original structure, and R_1 and R_3 represent the effect of aerodynamic force. In addition to the voltage relationships (12), the current relationship of the equivalent circuit can be obtained by rewriting the second equation of (1) as

$$i_{eq}(t) = C_p\dot{v}_p(t) + i_p(t) \tag{14}$$

where i_p is the electrical current flowing into the external energy harvesting circuit. Combining relationships (12) and (14) yields the equivalent circuit shown in Fig. 2, where the equivalent resistances R_1 and R_3 representing the effect of the aerodynamic force. Note it is a self-excited circuit with the negative resistance R_1 serving as an internal energy source or excitation to the circuit, and the positive resistance R_3 functioning as a variable, nonlinear resistance limiting the electrical current. Physically, the positive R_s represents the intrinsic mechanical damping of the piezo beam, the negative R_1 provides the excitation and power to induce and maintain the

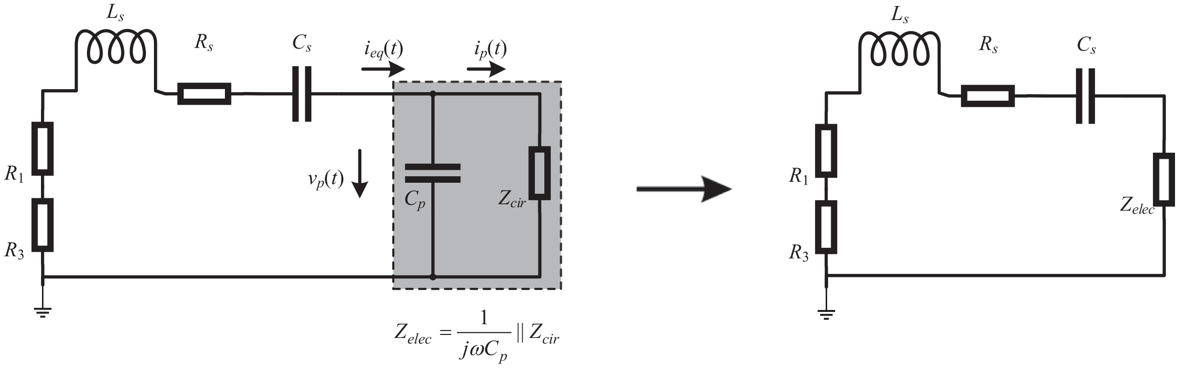

Fig. 2. Equivalent circuit diagram of a galloping piezoelectric energy harvester shunted to a general interface circuit.

galloping oscillations, and the positive R_3 represents an additional aerodynamic damping that restricts the structural response of the system, i.e., it increases with the structural response as shown in Eq. (13).

3. A unified model of galloping PEHs

With the equivalent circuit developed in Section 2.2, the power behavior of the system can be analyzed. First, denote the electrical impedance of the system in a general form as

$$Z_{elec} = R_{elec} + jX_{elec} \tag{15}$$

where R_{elec} and X_{elec} are the resistance and reactance components, respectively. The electrical impedance Z_{elec} represents the effect of both internal piezoelectric capacitance and external energy harvesting circuit, as shown by the shaded area in Fig. 2. It takes different forms for different energy harvesting interface circuits [35–37]. The general form used here is intended to represent all interface circuits for which an equivalent electrical impedance can be obtained. The equivalent impedance Z_{elec} (and its resistive and reactive components R_{elec}, X_{elec}) depends on the actual circuit load resistance (denoted as R for the rest of the paper). In other words, when the load resistance R is tuned, R_{elec} and X_{elec} change. The exact relation forms between these quantities will be discussed in detail in Section 4, where specific energy harvesting interface circuits are analyzed. To perform power analysis of the system, note that its equivalent circuit in Fig. 2 is self-excited without an explicit source. Therefore, the voltage drop of the entire closed-loop circuit must equal zero. Based on this relationship and the Kirchhoff's Voltage Law (KVL), we can have the following voltage equation in the frequency domain:

$$\left[j\omega L_s + R_s + R_1 + R_3 + \frac{1}{j\omega C_s} + Z_{elec}(j\omega)\right] i_{eq}(j\omega) = 0. \tag{16}$$

The terms inside the brackets as a whole must zero because the equivalent current i_{eq} cannot be zero when galloping takes place, resulting in the following relationship;

$$\begin{cases} \omega L_s - \dfrac{1}{\omega C_s} + X_{elec} = 0 \\ R_s + R_1 + R_3 + R_{elec} = 0 \end{cases}, \tag{17}$$

for the imaginary and real parts, respectively. Substituting the equivalent circuit element quantities in Eq. (13) into the above equations yields

$$\begin{cases} \omega^2 M - K + \omega\theta^2 X_{elec} = 0 \\ \dfrac{C}{\theta^2} - \dfrac{\rho LDUs_1}{2\theta^2} + \dfrac{3\rho LDs_3 r^2\omega^2}{8U\theta^2} + R_{elec} = 0 \end{cases} \tag{18}$$

The top part of Eq. (18) determines the vibration frequency ω of the system due to galloping. It can be seen that the actual galloping frequency depends on the original mechanical natural frequency of the GPEH, electromechanical coupling, and circuit tuning (through X_{elec}). The second part of Eq. (18) determines the structural response amplitude r, given the energy harvesting circuit and load characteristics, i.e., R_{elec} and X_{elec}.

The harvested power of the GPEH, i.e., dissipated in the external energy harvesting circuit, can be calculated by

$$P = i_{eq}^2 R_{elec} = |-\theta\dot{x}|^2 R_{elec} = \theta^2\omega^2 r^2 R_{elec}. \tag{19}$$

Interestingly, the product $\omega^2 r^2$ can be directly determined as a whole from the second part of Eq. (18) as

$$r^2\omega^2 = \frac{4\rho LDU^2 s_1 - 8UC - 8UR_{elec}\theta^2}{3\rho LDs_3}. \tag{20}$$

Substituting this result into Eq. (19) yields the harvested power expression for a GPEH in general:

$$P = \frac{\theta^2}{3\rho LDs_3}\left[\left(4\rho LDU^2 s_1 - 8UC\right)R_{elec} - 8U\theta^2 R_{elec}^2\right], \tag{21}$$

which shows that the harvested power depends on only the resistance component R_{elec} of the electrical impedance, not the reactance component X_{elec}. The direct effect of X_{elec} is on the galloping frequency of the system, as shown in the first equation of (18). It is interesting to note that, out of the three original mechanical parameters M, C, and K, only the damping term C is explicitly involved in the power expression Eq. (21). Therefore,

The most important characteristic of an energy harvester is the maximum possible power that can be harvested. To determine it, Eq. (21) can be rewritten by completing the square for R_{elec} as

$$P = \frac{8U\theta^4}{3s_3\rho LD}\left[-\left(R_{elec} - \frac{\rho LUDs_1 - 2C}{4\theta^2}\right)^2 + \left(\frac{\rho LUDs_1 - 2C}{4\theta^2}\right)^2\right] \tag{22}$$

It can be seen from the above expression that the power reaches its maximum when the resistive component of the electrical impedance is optimized at

$$R_{elec}^{opt}=\frac{\rho LUDs_1-2C}{4\theta^2},\tag{23}$$

yielding the optimal power

$$P_{opt}=\frac{8U\theta^4}{3s_3\rho LD}\left(\frac{\rho LUDs_1-2C}{4\theta^2}\right)^2.\tag{24}$$

This optimal power represents the maximum possible power that can be harvested by the galloping PEH for a given wind speed through the tuning of the circuity, i.e., the power limit. Its expression (24) can be simplified further and defined as the *power limit* of the system as

$$P_{lim}=\frac{U(\rho LUDs_1-2C)^2}{6s_3\rho LD}.\tag{25}$$

Equation (25) shows that the power limit of GPEHs is not inversely proportional to the mechanical damping ratio as for vibration-based PEHs [43], but through a more complicated second-order relationship. It is important to emphasize that this power limit can be reached *only* when the condition (23) on the electrical impedance is satisfied. However, physical circuits impose constraints on the attainable range of R_{elec} through the tuning of circuit load resistance R. The electromechanical coupling of the system has to be equal or greater than a critical value, i.e., critical coupling, to make it possible to satisfy the condition. This is graphically illustrated in Fig. 3,

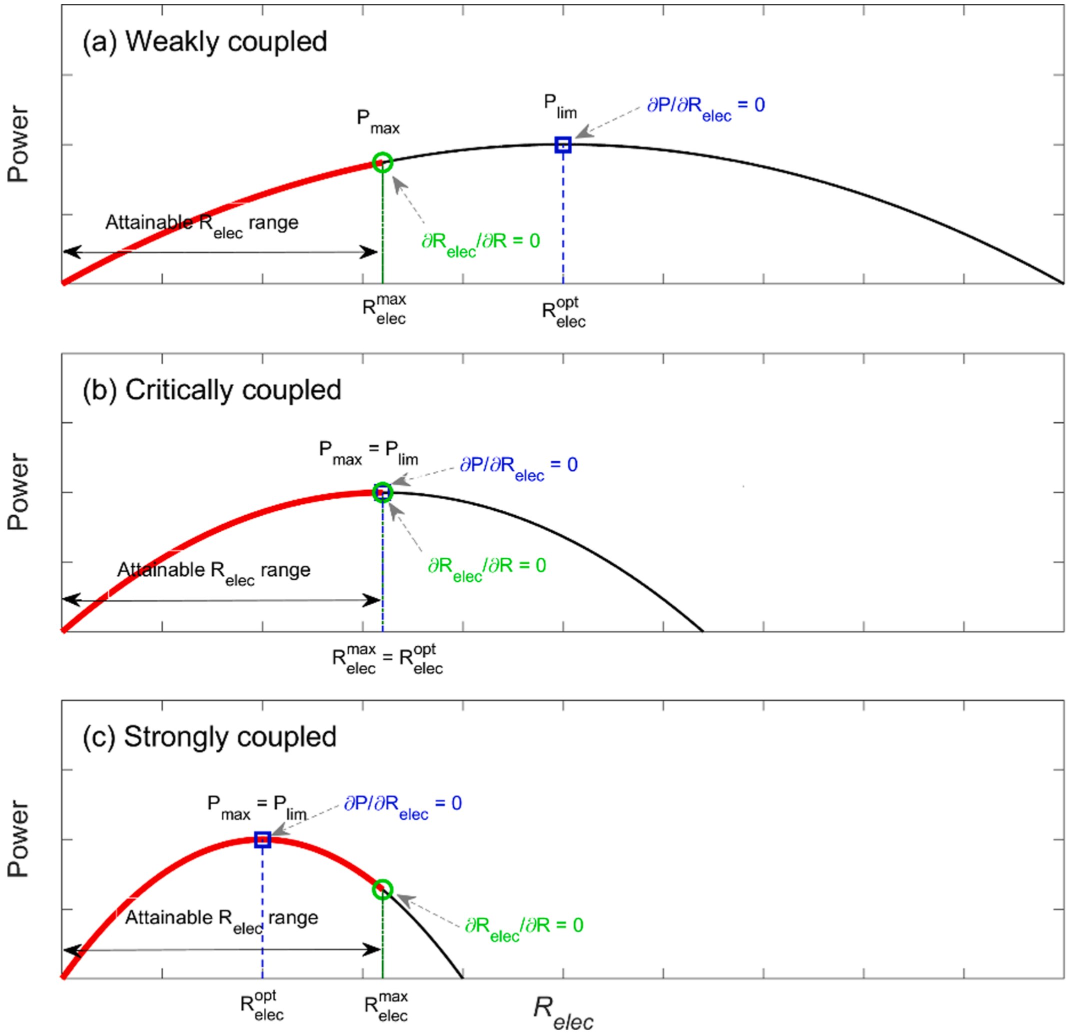

Fig. 3. Harvested power vs. resistive component R_{elec} of electrical impedance Z_{elec} at various coupling level. (a) Weakly coupled; (b) critically coupled; (c) strongly coupled. R_{elec}^{opt}: optimal R_{elec} for power limit; R_{elec}^{max}: maximum attainable R_{elec} through circuit tuning.

where the overall trend of the harvested power in Eq. (22) against R_{elec} is plotted. Through the tuning of load resistance R, only a finite range of R_{elec}, i.e., [0 R_{elec}^{max}], can be attained due to physical constraints. Weakly coupled systems, e.g., Fig. 3(a), have a small coupling coefficient θ. As a result, the optimal R_{elec} for power limit, i.e., R_{elec}^{opt} as indicated by the vertical blue dashed line, is large as given by Eq. (23) and falls outside the attainable R_{elec} range, making it not possible to reach the power limit P_{lim} through tuning. As a result, the achievable maximum power P_{max} occurs at R_{elec}^{max} but is lower than P_{lim}. As the coupling increases, R_{elec}^{opt} decreases. Graphically, the blue dashed line moves to the left. The instant $R_{elec}^{opt} = R_{elec}^{max}$ corresponds to a critically coupled situation as illustrated in Fig. 3(b) and $P_{max} = P_{lim}$. The associated coupling is the minimum coupling required to make it possible for the system power to reach P_{lim} through circuit (or load resistance) tuning, which is termed as the *critical coupling*. Further increase of the coupling beyond this critical coupling results in a strongly coupled situation as shown in Fig. 3(c). In this case, R_{elec}^{opt} is small due to a large coupling coefficient θ (see Eq. (23)), and it is able to fall into the attainable R_{elec} now. As a result, it is possible for the maximum power P_{max} to reach P_{lim} through the circuit or load resistance tuning. Note though that the maximum power occurs at R_{elec}^{opt}, which is different from (smaller than)R_{elec}^{max}. As an additional note, the attainable R_{elec} range depends on the type of energy harvesting interface circuit. Therefore, the critical coupling requirement is different for different interface circuits as well. To determine the critical coupling, note that graphically from Fig. 3(b), the system is of critical coupling when the maximum attainable R_{elec} is equal to the optimal R_{elec} for power limit given by Eq. (23):

$$R_{elec}^{max} = R_{elec}^{opt}. \tag{26}$$

This will be used as the governing relationship to find the critical coupling for various energy harvesting interface circuits in Section 4.2, where the power characteristics of galloping PEHs of various interface circuits are discussed and compared.

A mathematical perspective on the relationship between the maximum power and power limit, along with the effect of coupling, can be obtained by differentiating the general power expression (22) with respect to the circuit load resistance R and setting it to zero:

$$\frac{\partial P}{\partial R} = \frac{\partial P}{\partial R_{elec}}\frac{\partial R_{elec}}{\partial R} = -\frac{16U\theta^4}{3s_3\rho LD}\left(R_{elec} - \frac{\rho LUDs_1 - 2C}{4\theta^2}\right)\frac{\partial R_{elec}}{\partial R} = 0. \tag{27}$$

Note that the chain rule has been used in the above equation since the power expression given in Eq. (21) is not explicitly in terms of R, but the electrical resistance R_{elec} instead. Equation (27) gives the condition on local (and possibly global) maximum or minimum of the power. In this case, there are two mathematical solutions:

$$R_{elec} - \frac{\rho LUDs_1 - 2C}{4\theta^2} = 0 \text{ or } \frac{\partial R_{elec}}{\partial R} = 0 \tag{28}$$

Physically, the first solution corresponds to the situation that the system is tuned toR_{elec}^{opt} to reach the power limit as given by Eq. (22), i.e., $\partial P/\partial R_{elec} = 0$; while the second solution corresponds to the situation that the system is tuned to the maximum attainable R_{elec} denoted as R_{elec}^{max}, i..e, $\partial R_{elec}/\partial R = 0$. Note that since the power P is plotted versus R_{elec} in Fig. 3, the location of $\partial P/\partial R_{elec} = 0$, i.e., the power limit location, is the zero-slope location on the power curve. On the other hand, the location of $\partial R_{elec}/\partial R = 0$ is at the right end of the attainable range of R_{elec}, where R_{elec} reaches its maximum through the tuning of circuit load resistance R. Fig. 3(c) shows that, if the coupling is greater than the critical coupling, i.e., strongly coupled, the first solution in Eq. (28), i.e., $\partial P/\partial R_{elec} = 0$, is possible and power can reach the global maximum power P_{lim} at R_{elec}^{opt}; while the power at R_{elec}^{max}, corresponding to the second solution $\partial R_{elec}/\partial R = 0$, is a local minimum. In the case of weak coupling shown in Fig. 3(a), the first solution in Eq. (28) is not achievable, and the second solution is the only viable one. The circuit load resistance R is tuned to maximize R_{elec} and the maximum power occurs at R_{elec}^{max}. In the case of critical coupling shown in Fig. 3(b), both solutions in Eq. (28) exist and occur at the same circuit load resistance R. Additional discussions on the relationship between P, R_{elec}, and R, along with the significance of the two zero-partial derivative solutions in Eq. (28) will be provided in Section 4.2.1, where the power P is directly plotted against the circuit load resistance R in the case of a purely

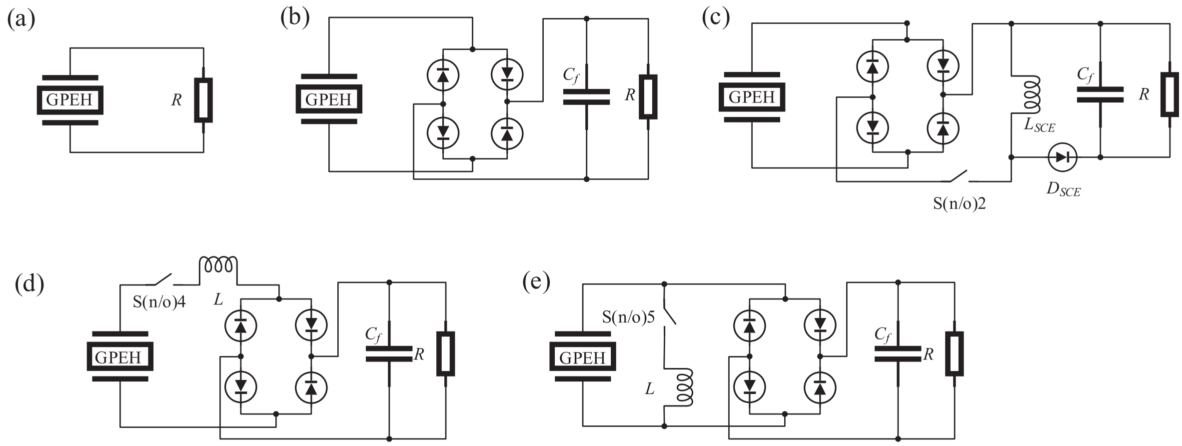

Fig. 4. Different energy harvesting interface circuits: (a) AC, (b) SEH, (c) SCE, (d) S-SSHI, (e) P-SSHI.

resistive energy harvesting interface circuit.

It is important to point out that we did not assume the exact type of energy harvesting interface circuit in the derivation of the equivalent circuit and the power analysis after it. In other words, the results are general and can be applied to any type of energy harvesting interface circuits as long as it can be accurately represented by an electrical impedance expression as in Eq. (15). This is possible for any linear circuits and also few representative nonlinear rectified circuits with known equivalent electrical impedance representations. Hence, the equivalent circuit and the power expressions obtained in this Section provide a framework and model that unifies galloping PEHs of different energy harvesting interface circuits based on the equivalent electrical impedance concept. It serves as a systematic approach for analysis and comparison. In the next section, power behavior of GPEHs of few typical circuit interfaces are discussed, such as resistive (AC), standard AC/DC (SEH), synchronized charge extraction (SCE), and synchronized switch harvesting on inductor (SSHI). As they are governed by the same unified model, they share some common characteristics. On the other hand, the difference in the circuit configuration also leads to unique characteristics in their behavior. All of these will be discussed in detail in the next section.

4. Power characteristics of a conventional GPEH with different interface circuits

4.1. Different interface circuits and numerical simulation method

Fig. 4 shows five representative circuits widely used in galloping energy harvesting, including the AC, SEH, SCE, and S-SSHI/P-SSHI circuits. Notably, the analytical solutions of a conventional GPEH with the AC, SHE, and SCE interface circuits have been derived by Zhao et al. [37] by directly manipulating system governing equations and treating the circuits individually. The drawback of the method is that it required tediously long derivation for each circuit, and the solutions are separately given which failed to highlight important connections between these circuits. To this end, the unified model is employed in analyze the performance of this conventional GPEH with these five circuits. The parameters used in this paper are the same as the experimental results in Ref. [24], as shown in Table 1. In the following section, the proposed unified model is employed to obtain the analytical solutions. Note that the solutions for the AC, AC/DC and SCE interface circuits are consistent with those obtained by Zhao et al. [37]; while the solutions for the SSHI circuits are newly presented for the first time.

4.2. Analytical solutions of various interface circuits

4.2.1. Resistive circuit (AC)

The electrical impedance of a PEH of an AC interface circuit has been determined [43] as

$$Z_{elec}^{AC} = R_{elec}^{AC} + jX_{elec}^{AC} = \frac{R}{1 + (\omega C_p R)^2} - j\frac{\omega C_p R^2}{1 + (\omega C_p R)^2}. \tag{29}$$

By submitting Eq. (29) into Eqs. (18) and (19) of the unified model, the analytical solution of GPEH with AC interface is obtained. The resistance component of the electrical impedance (Eq. (29)) is given as

$$R_{elec}^{AC} = \frac{R}{1 + (\omega C_p R)^2}, \tag{30}$$

which changes between zero and a maximum as the electrical load is tuned. As discussed in Section 3, this component directly affects the harvested power, and it is important to determine its maximum and associated conditions. Mathematically, this can be done by differentiation of Eq. (30). However, the variables ω and R are dependent because the vibration frequency ω depends on the electrical load R as shown in Eq. (18). In other words, ω changes as the electrical load R changes. However, this change is usually small, within a narrow range between the short-circuit and open-circuit natural frequencies of the system. As a result, ω can be assumed to be almost constant with respect to R. Under this assumption, setting the first derivative of Eq. (30) to zero yields the optimal electrical load resistance that maximizes R_{elec}:

$$R_{opt} = \frac{1}{\omega C_p} \tag{31}$$

with the maximum

Table 1
Parameters of galloping piezoelectric energy harvester.

Mechanical/Electrical parameters		Aerodynamic parameters	
Effective mass m_1 (g)	113.4	Air Density, ρ (kg/m^3)	1.24
Effective stiffness k_1 (N/m)	58.02	Bluff body height, L (m)	0.1
Damping ratio ζ_1	0.003	Cross flow dimension, D (m)	0.05
Capacitance C_p (nF)	187	Linear aerodynamic coefficient, s_1	2.5
		Cubic aerodynamic coefficient, s_3	130

$$\left(R_{elec}^{AC}\right)_{max} = \frac{1}{2\omega C_p} \tag{32}$$

Fig. 5 illustrates graphically how the power and impedance components change as the load resistance increases. The electromechanical coupling has a strong impact on the behavior as shown by the power curves in Fig. 5(a,c,e), where k^2 is the electromechanical coupling coefficient of the system defined by $k^2 = \theta^2/(KC_p)$. In the case of weak coupling, e.g., $k^2 = 0.004$, the power initially increases with the load resistance, and then decreases once the load resistance becomes too large. Note that the maximum power is still below the power limit as denoted by the horizontal dashed line in purple, whose value is given by Eq. (25). In the case of critical coupling, e.g., $k^2 = 0.0061$, the power curve is similar to that for weak coupling. However, the power is able to just reach the power limit at one location (with one particular load resistance). If the coupling increases further, e.g., $k^2 = 0.008$, the system becomes strongly coupled, and the

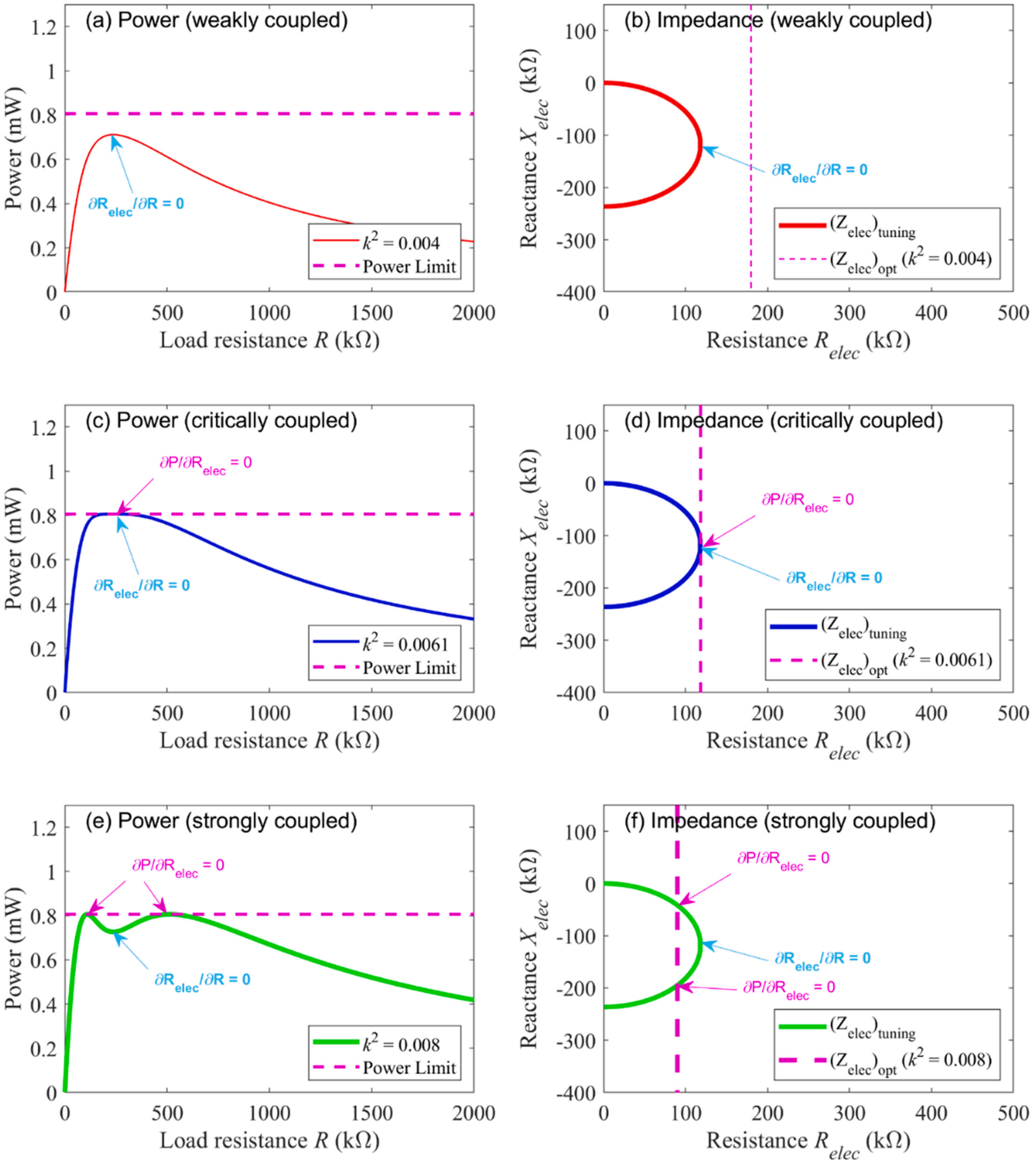

Fig. 5. Power and impedance plots of GPEH with AC circuit at various levels of electromechanical coupling: (a-b) weakly coupled; (c-d) critically coupled; (e-f) strongly coupled.

power reaches the power limit at two load resistances. Note that regardless of the value of coupling and load resistance, the overall maximum power is always less or equal to the power limit. More insights into the relationship between power and load resistance can be attained through the method of impedance plot, which presents the relationship between the (mechanical) source and (electrical) tuning impedances graphically [43,44]. For instance, in Fig. 5(b), as the load resistance increases, the corresponding impedance point (refer to Eq. (29)) moves along the tuning impedance curve (the arc shape) in the clockwise direction from the origin. The vertical dashed line (termed matched impedance or power limit line) represents the *required* optimal R_{elec} to reach the power limit. The distance between the tuning impedance point and the power limit line can be used as an indicator of the power level qualitatively: a shorter distance indicates a higher power [49]. When the tuning impedance curve and power limit line intersect, the power limit is reached. When the coupling is weak, e.g., $k^2 = 0.004$, the matched impedance curve (in red) is away from the tuning impedance curve. Therefore, the power limit is not reached and the maximum power occurs at R_{elec}^{max}. To relate to the discussions in Section 3 (in particular, Eqs. (27–28)), this maximum power location in the case of weak coupling is also where $\partial R_{elec}/\partial R = 0$, i.e., the second solution of Eq. (27). The first solution is not possible due to low electromechanical coupling. When the coupling is strong, e.g., $k^2 = 0.008$, Fig. 5(f) shows the tuning and matched impedance curves are able to intersect at two locations, where the first solution of Eq. (27) exists, i.e., $\partial P/\partial R_{elec} = 0$. This leads to two power limit peaks on the power curve as in Fig. 5(e). In addition, the location of $\partial R_{elec}/\partial R = 0$ is a local minimum on the curve. The state of critical coupling occurs when the tuning impedance curve and power limit line are just “touching” each other as shown in Fig. 5(d) for $k^2 = 0.0061$. The associated power curve in Fig. 5(c) has just one power limit peak, where $\partial P/\partial R_{elec} = \partial R_{elec}/\partial R = 0$.

The critical coupling can be determined by noting that at this state, the maximum R_{elec} is equal to the optimal R_{elec}, as given by Eq. (26) and illustrated in Fig. 3(b) and 5(d). In the case of a resistive (AC) interface circuit, substituting expressions (23) and (32) into Eq. (26) yields

$$\frac{1}{2\omega C_p} = \frac{\rho LUDs_1 - 2C}{4\theta^2}, \qquad \text{33)}$$

from which we have

$$\theta_c^2 = \omega C_p \left(\frac{1}{2}\rho LUDs_1 - C\right) \tag{34}$$

It is more common to use the coupling coefficient k^2 instead of the coupling constant θ to represent the overall electromechanical coupling of a system, which is defined as

$$k^2 = \frac{\theta^2}{KC_p}. \tag{35}$$

Combining expression (34) and (35) yields the critical coupling coefficient for GPEHs of a resistive AC interface circuit:

$$\left(k_c^2\right)_{AC} = \frac{\omega}{2K}(\rho LUDs_1 - 2C) \tag{36}$$

4.2.2. Standard AC-DC circuit (SEH)

The electrical impedance of a PEH of a standard AC-DC interface circuit has been determined [43] as

$$Z_{elec}^{SEH} = \frac{2R}{\left(\omega C_p R + \pi/2\right)^2} - j\frac{R}{\omega C_p R + \pi/2}. \tag{37}$$

The resistance component of the electrical impedance is given as

$$R_{elec}^{SEH} = \frac{2R}{\left(\frac{\pi}{2} + \omega C_p R\right)^2}. \tag{38}$$

By differentiating expression (38) with respect to R, the load resistance to maximizes (38) can be found to be

$$R_{opt}^{SEH} = \frac{\pi}{2\omega C_p}. \tag{39}$$

Substituting Eq. (39) into Eq. (38) yields the maximum attainable R_{elec} through circuit tuning:

$$\left(R_{elec}^{SEH}\right)_{max} = \frac{1}{\pi\omega C_p}. \tag{40}$$

To find the critical coupling in this case, substituting (23) and (40) into Eq. (26), we have

$$\frac{1}{\pi\omega C_p} = \frac{\rho LUDs_1 - 2C}{4\theta^2}, \tag{41}$$

from which the critical coupling coefficient can be found to be

$$\left(k_c^2\right)_{SEH} = \frac{\theta_c^2}{KC_p} = \frac{\pi}{4}\frac{\omega}{K}(\rho LUDs_1 - 2C) \tag{42}$$

Fig. 6 shows the power and impedance plots of the GPEH with a SEH circuit, which are similar to those for the AC interface circuit. For weak coupling, there is no intersection in the impedance plot, and there is only one power peak (below the power limit) on the power curve. In the case of critical coupling, there is one intersection location in the impedance plot. The power curve still has just one power peak but it is at the power limit now. In the case of strong coupling, there are two intersection points in the impedance plot. Correspondingly, there are two power limit peaks on the power curve. Note that given the same configuration of the GPEH, the SEH circuit requires a higher critical coupling coefficient than that for the AC circuit, in this case, 0.0096 vs. 0.0061. Their general relationship can be seen by comparing Eqs. (36) and (42). This will be discussed further in Section 4.3.

4.2.3. *Synchronized charge extraction (SCE)*

The electrical impedance of a PEH of an SCE interface circuit has been determined [50] as

$$Z_{elec}^{SCE} = R_{elec}^{SCE} + jX_{elec}^{SCE} = \frac{1}{\omega C_p}\left(\frac{4}{\pi} - j\right). \tag{43}$$

The resistance component of the electrical impedance is given as

$$R_{elec}^{SCE} = \frac{4}{\pi}\frac{1}{\omega C_p}, \tag{44}$$

which is a constant. To find the critical coupling in this case, substitute (23) and (44) into Eq. (26) and we have

$$\frac{4}{\pi\omega C_p} = \frac{\rho LUDs_1 - 2C}{4\theta^2}, \tag{45}$$

from which the critical coupling coefficient can be found to be

$$\left(k_c^2\right)_{SCE} = \frac{\theta_c^2}{KC_p} = \frac{\pi}{16}\frac{\omega}{K}(\rho LUDs_1 - 2C) \tag{46}$$

Fig. 7 shows the power and impedance plots of the GPEH with a SCE interface circuit. Since the electrical impedance is independent of the load resistance *R*, the output power stays constant regardless of the load resistance. This special feature enables a stable output power in the circumstance where resistance load changes a lot. However, it is noted in Fig. 7(b) that the tuning impedance Z_{elec} is a single point and intersection takes place only in the case of critical electromechanical coupling. As a result, when the coupling is larger or lower than the critical coupling, the maximum power is lower than the power limit. In other words, the piezoelectric transducer should be carefully designed to attain the critical coupling and power limit. However, it is also shown in Eq. (46) that the critical coupling of the SCE circuit is proportional to the wind speed *U*. Thus, for a fixed eletromechanical coupling, the power limit can be achieved at a certain wind speed, which means that the condition of SCE circuit to obtain power limit is quite oppressive.

4.2.4. *P-SSHI, S-SSHI circuits*

The electrical impedance of SSHI interface circuits is given [51] as

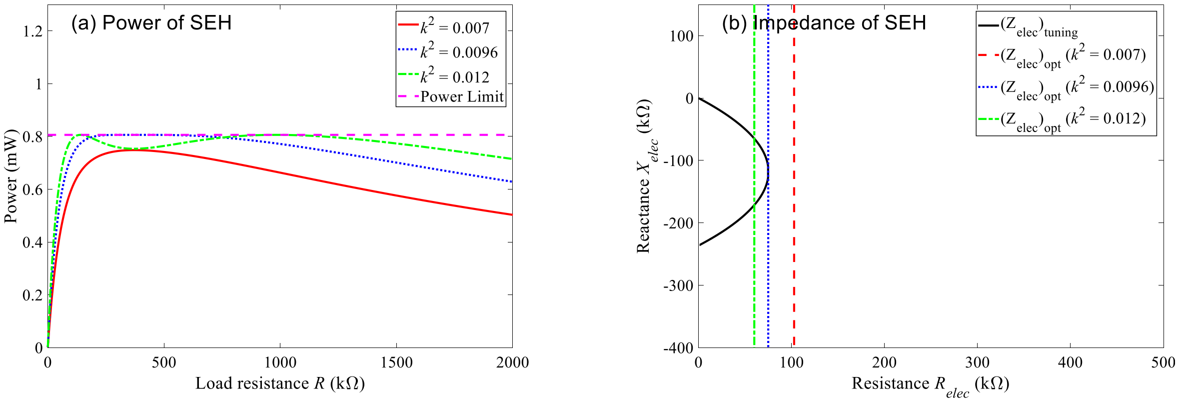

Fig. 6. The power performance of GPEH with DC circuit: (a) effect of k^2 on the relation between load resistance and power, (b) impedance plot.

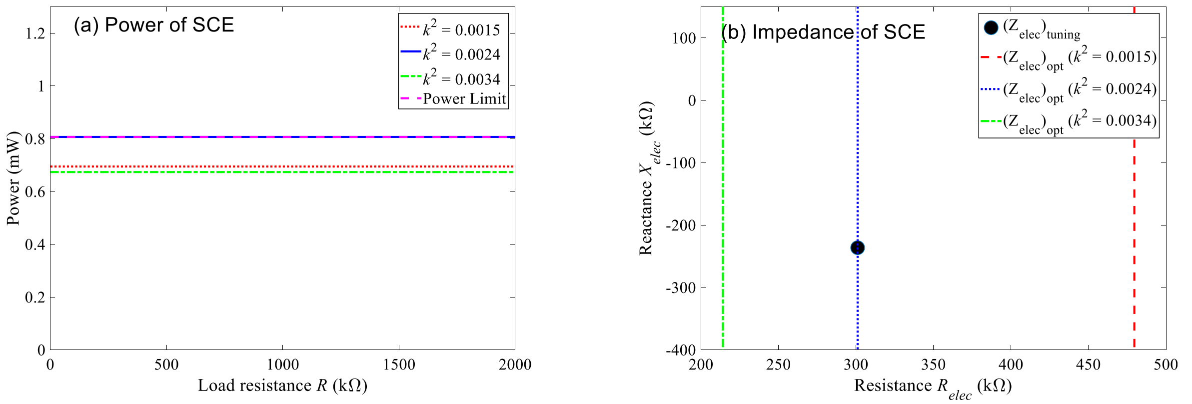

Fig. 7. Power performance of GPEH with SCE circuit: (a) effect of k^2 on the relation between load resistance and power, (b) impedance plot.

$$\begin{cases} Z_{elec}^{S-SSHI} = \dfrac{\dfrac{2}{\omega C_p}}{\dfrac{\pi}{2}\dfrac{1-\gamma}{1+\gamma}+C_p\omega R} - j\dfrac{1}{\omega C_p} \\ Z_{elec}^{P-SSHI} = \dfrac{2R\left[1+\dfrac{1-\gamma^2}{2\pi}C_p\omega R\right]}{\left(\dfrac{\pi}{2}+\dfrac{1-\gamma}{2}C_p\omega R\right)^2} - j\dfrac{\dfrac{1-\gamma}{2}R}{\dfrac{\pi}{2}+\dfrac{1-\gamma}{2}C_p\omega R} \end{cases}, \tag{47}$$

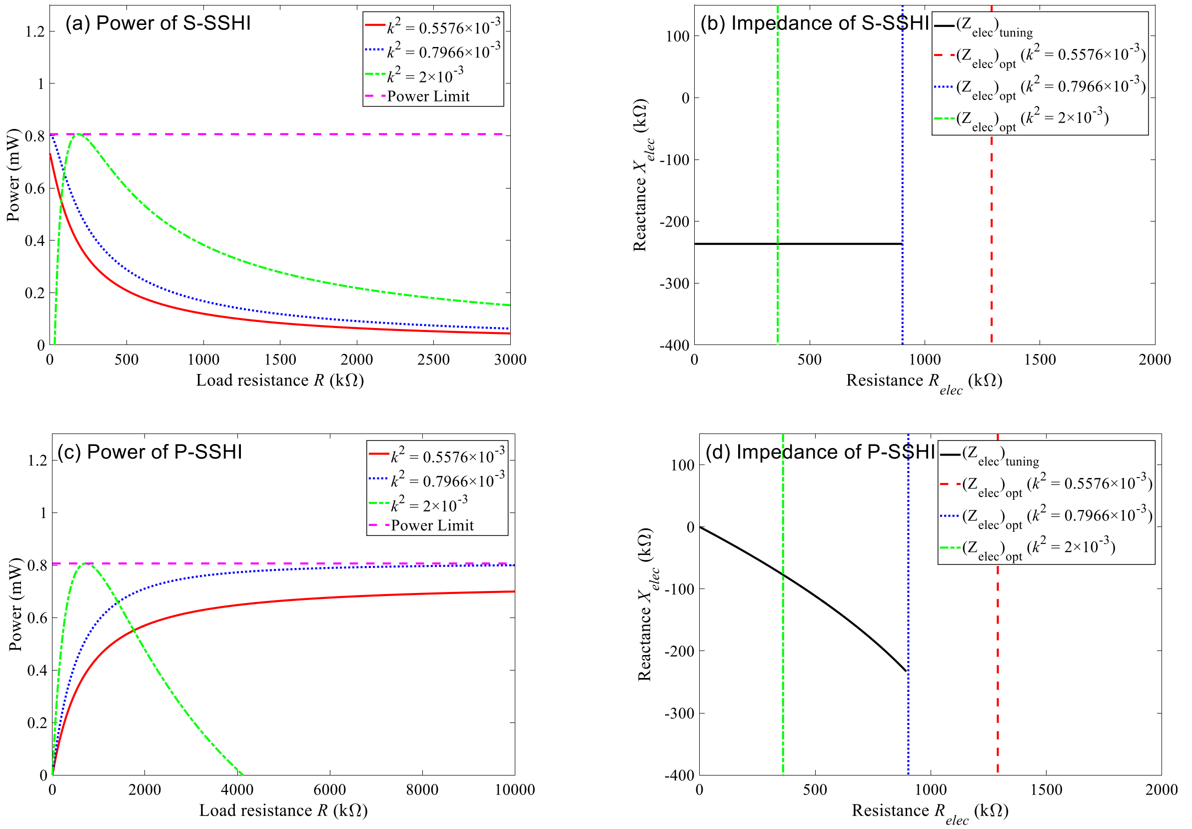

Fig. 8. Power performance of GPEH with SSHI circuit ($\gamma = 0.5$): (a) effect of k^2 on the relation between load resistance and power of S-SSHI, (b) impedance plot of S-SSHI, (c) effect of k^2 on the relation between load resistance and power of P-SSHI, (d) impedance plot of P-SSHI,

where γ is the inversion factor of the circuit. It can be shown that $R_{elec}^{S-SSHI}$is maximized at $R = 0$, and $R_{elec}^{P-SSHI}$is maximized at $R = \infty$. The maximized expressions are the same at

$$\left(R_{elec}^{SSHI}\right)_{max} = \frac{4}{\pi\omega C_p}\frac{1+\gamma}{1-\gamma}. \tag{48}$$

By submitting Eq. (47) into Eqs. (18) and (19) of the unified model, the analytical solution of GPEH with a SSHI interface circuit is obtained. To find the critical coupling, again, we substitute Eqs. (23) and (48) into Eq. (26) and have

$$\frac{4}{\pi\omega C_p}\frac{1+\gamma}{1-\gamma} = \frac{\rho LUDs_1 - 2C}{4\theta^2}, \tag{49}$$

from which the critical coupling coefficient can be obtained as

$$\left(k_c^2\right)_{SSHI} = \frac{\pi}{16}\frac{1-\gamma}{1+\gamma}\frac{\omega}{K}(\rho LUDs_1 - 2C) \tag{50}$$

Fig. 8 depicts the power and impedance plots of these two types of SSHI circuits. The circuits share some similarities in their system behavior. There is only one power peak for both weak coupling and strong coupling conditions. This is consistent with the observation that the tuning impedance curve and power limit line intersect at one location even with strong coupling. The critical electromechanical coupling for the P-SSHI and S-SSHI circuits is the same due to the fact that they have the same R_{elec}^{max}. On the other hand, some differences between the two circuits are also observed. First, in the weak coupling condition (curves in red), the power of S-SSHI is maximized at $R = 0$; while the power of P-SSHI is maximized at $R = \infty$. Second, in the strong coupling condition (curves in green), the power of S-SSHI is very low when the resistance is close to zero; while that of P-SSHI is low when the resistance is close to infinite. The impedance plot provides an easy and effective way to understand these observations. Take S-SSHI as an example with impedance plot Fig. 8(b). As the load resistance R increases from 0 to ∞, the resistance component of the tuning impedance decreases as given by Eq. (47). Graphically, the tuning impedance point moves from the furthest point on the right to the left. If the system is weakly coupled, the tuning impedance point starts at a location away from the power limit line in red and moves further and further away. As a result, the power starts below the power limit and keeps decreasing. Similarly, if the system is critically coupled, the power starts at the power limit and keeps decreasing. If the system is strongly coupled, the tuning impedance point starts at a location to the right of the power limit line (in green) and moves to the left as R increases. As the distance decreases, the power increases until the power limit is reached (when the tuning impedance point reaches the power limit line). As the tuning impedance point continues moving to the left and away from the power limit line, the power decreases. The same approach and analysis can be applied to the P-SSHI interface circuit. The major difference though, is that the tuning impedance point starts from the origin and moves to the right when the load resistance increases from 0 to ∞.

4.3. Performance comparison

4.3.1. Optimal load, maximum power and critical electromechanical coupling

The above section derives the analytical solutions of GPEHs connected with various interface circuits based on the unified model. The results are summarized and compared in this section. First, the power output of a conventional GPEH is given by Eq. (18). From this equation, it is learned that the output power mainly depends on the resistance component R_{elec} of the electrical impedance representing the interface circuit. Systems of weak coupling (where the power limit is not reached) are very common in practice. In this case, a larger R_{elec} leads to higher output power. Thus, the R_{elec} of these interface circuits should be compared to find out which circuit has the highest output power in the weak coupling situation. In the case of strong coupling (where the power limit is reached), it is reasonable to compare the critical electromechanical coupling (k^2) of these circuits since the lower of k^2 means the less piezoelectric materials required to attain the power limit. For these purposes, Table 2 compares the electrical resistance R_{elec} and critical electromechanical coupling k^2 of these circuits. It is clearly shown that the electrical resistances R_{elec} in the order from the small to the large are: SEH, AC, SCE, and S/P-SSHI. Hence, it is indicated that the SEH circuit has the lowest output power while the S/P-SSHI circuits

Table 2
Electrical resistance components and critical coupling coefficients of various interface circuits.

Interface circuits	R_{elec}	Value	k_c^2	Value
AC	$\left(R_{elec}^{AC}\right)_{max}$	$\frac{1}{2}\frac{1}{\omega C_p}$	$\left(k_c^2\right)_{AC}$	$\frac{1}{2}\frac{\omega}{K}(\rho LUDs_1 - 2C)$
SEH	$\left(R_{elec}^{SEH}\right)_{max}$	$\frac{1}{\pi}\frac{1}{\omega C_p}$	$\left(k_c^2\right)_{SEH}$	$\frac{\pi}{4}\frac{\omega}{K}(\rho LUDs_1 - 2C)$
SCE	R_{elec}^{SCE}	$\frac{4}{\pi}\frac{1}{\omega C_p}$	$\left(k_c^2\right)_{SCE}$	$\frac{\pi}{16}\frac{\omega}{K}(\rho LUDs_1 - 2C)$
S-SSHI	$\left(R_{elec}^{S-SSHI}\right)_{max}$	$\frac{1+\gamma}{1-\gamma}\frac{4}{\pi}\frac{1}{\omega C_p}$	$\left(k_c^2\right)_{S-SSHI}$	$\frac{\pi}{16}\frac{1-\gamma}{1+\gamma}\frac{\omega}{K}(\rho LUDs_1 - 2C)$
P-SSHI	$\left(R_{elec}^{P-SSHI}\right)_{max}$	$\frac{1+\gamma}{1-\gamma}\frac{4}{\pi}\frac{1}{\omega C_p}$	$\left(k_c^2\right)_{P-SSHI}$	$\frac{\pi}{16}\frac{1-\gamma}{1+\gamma}\frac{\omega}{K}(\rho LUDs_1 - 2C)$

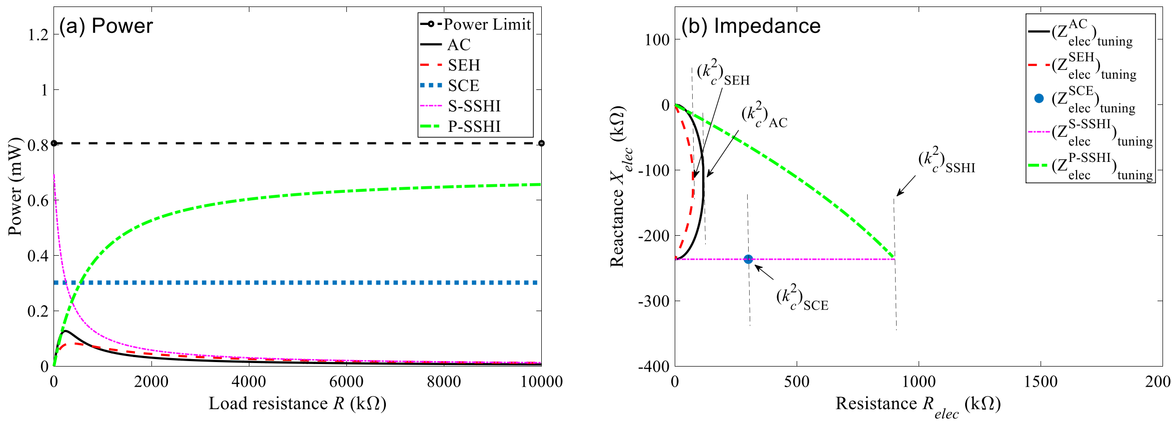

Fig. 9. Comparing the performance of various circuits (a) power plot, $k^2 = 0.0005$, weakly coupled, (b) impedance plot.

have the highest power in the case of weak coupling. For validation, the relations of resistance and power of these circuits when the electromechanical coupling is very small ($k^2 = 0.0005$) are calculated and plotted in Fig. 9(a). Subsequently, the critical couplings of these circuits are compared by using the impedance plot in Fig. 9(b) and Table 2. It is clearly shown that the critical coupling coefficients in the order from smallest to largest are: S/P-SSHI, SCE, AC, SEH. Thus, the S/P-SSHI circuits require the lowest coupling to attain the power limit. This is consistent with the highest power they achieve in Fig. 9(a). The low coupling requirement is advantageous for piezoelectric transducers in energy harvesting applications.

4.3.2. Cut-in wind speed of a conventional GPEH with various interface circuits

In addition, the unified model can be used to determine and compare the cut-in wind speed of GPEHs connected with the five interface circuits. Note that the power equation (21) is quadratic in terms of the wind speed U with two roots

$$U_1 = 0, U_2 = \frac{2}{\rho L D s_1}\left(C + \theta^2 R_{elec}\right) \tag{51}$$

Since the coefficient before the U^2 term in Eq. (21) is positive, if the wind speed falls between the two roots, the power P would be negative mathematically. This is not physically possible, but means that the galloping motion does not take place. For the power to be positive or the galloping motion to occur, the wind speed should be greater than U_2. In other words, U_2 is the cut-in wind speed in general, which can be rewritten as

$$U_{cut-in} = \frac{2M\omega_n}{\rho L D s_1}\left(\zeta + k^2\omega_n C_p R_{elec}\right) \tag{52}$$

which provides a unified, explicit expression of the cut-in wind speed. First, the cut-in wind speed increases with the mechanical damping and electromechanical coupling of the system (associated with the induced electrical damping due to energy harvesting [52]), both of which restrict the system's structural motion and make it more difficult for the galloping motion to initiate. Secondly, the cut-in speed can be determined by simply substituting the R_{elec} expression of the interface circuit of interest into Eq. (52). For convenience, Table 3 summarizes the R_{elec} expression of various interface circuits for the cut-in speed calculation. Thirdly, the cut-in speed depends on the load resistance and increases with R_{elec}. By referring to Fig. 9(b), in the case of a weakly coupled system (fairly common

Table 3
Cut-in wind speed of a GPEH connected with various interface circuits.

Interface circuits	R_{elec}	Value	U_{cut-in}
AC	R^{AC}_{elec}	$\frac{R}{1+(\omega C_p R)^2}$	$\frac{2}{\rho L D s_1}\left(C + \theta^2 R_{elec}\right)$
SEH	R^{SEH}_{elec}	$\frac{2R}{(\pi/2+\omega C_p R)^2}$	
SCE	R^{SCE}_{elec}	$\frac{4}{\pi}\frac{1}{\omega C_p}$	
S-SSHI	R^{S-SSHI}_{elec}	$\frac{2}{\omega C_p}\frac{1}{\frac{\pi}{2}\frac{1-\gamma}{1+\gamma}+C_p\omega R}$	
P-SSHI	R^{P-SSHI}_{elec}	$\frac{2R\left[1+\frac{1-\gamma^2}{2\pi}C_p\omega R\right]}{\left(\frac{\pi}{2}+\frac{1-\gamma}{2}C_p\omega R\right)^2}$	

in practice), the maximum power output is obtained by tune the circuit to an impedance point on the farthest point on the right, where R_{elec} is maximized. Under this condition, i.e., the load resistance is tuned for maximum power, the cut-in speeds for different interface circuits are different and they are related as $U^{SEH}_{cut-in} < U^{AC}_{cut-in} < U^{SCE}_{cut-in} < U^{SSHI}_{cut-in}$, essentially following the same order as their R_{elec} values. Note that the results agree with those obtained by Zhao et al. in [37]. However, Eq. (52) provides a unified, general expression of the cut-in wind speed that can be used conveniently. It highlights important system parameters that directly affects the cut-in wind speed, and helps understand the similarity and difference between the various interface circuits.

5. Conclusions

This paper proposes a novel impedance analysis framework for galloping based energy harvesters. First, a general, self-excited equivalent circuit is developed to represent GPEHs. Next, with the aid of equivalent impedance analysis, a unified model is obtained to unify various types of energy harvesting interface circuits and structures. The optimal load, maximum power, power limit, and critical electromechanical coupling are then conveniently obtained for both linear and nonlinear GPEHs. This method is applied to a conventional (linear) GPEH with a general interface circuit (represented by a general equivalent impedance) to study the common behavior of GPEHs even if connected with various interface circuits. After that, detailed studies are performed on GPEHs connected with five particular energy harvesting interface circuits to investigate their unique behaviors. A comprehensive comparison is conducted to evaluate the performance of these circuits on enhancing the energy harvesting capability of a conventional GPEH. Subsequently, this method is applied to a monostable GPEH to demonstrate its feasibility for the analysis of nonlinear GPEHs. From the study, several important conclusions are drawn as follows:

1) For the conventional GPEH, it is revealed that the power limit is independent of the type of energy harvesting circuit. In the case of weak coupling, it is found that the SEH interface circuit has the lowest output power while the S/P-SSHI circuits have the highest power.
2) As for the critical electromechanical coupling of a conventional GPEH, it is shown that the critical couplings in the order from smallest to largest are: S/P-SSHI, SCE, AC, SEH. The S/P-SSHI circuits require the lowest electromechanical coupling to reach the power limit, which is beneficial to reduce the requirement of piezoelectrical material in real applications.
3) Equation (21) is the foundation of the unified model, which can be used to calculate the power of GPEHs. The critical coupling results summarized in Table 2 and the cut-in wind speed results in Table 3 are applicable to both types of GPEHs too.

Finally, it is important to point out the limitation of this work and associated results. A major element of the proposed model is the equivalent impedance representing the nonlinear interface circuit. However, the equivalent impedance was obtained through a Fourier series approximation of the actual nonlinear waveform of the system [41]. In addition, dielectric loss in the circuits has been neglected in the analysis, which could be significant and deteriorate the actual power performance [53,54].

CRediT authorship contribution statement

Chunbo Lan: Methodology, Software, Writing – original draft, Investigation. **Yabin Liao:** Conceptualization, Methodology, Writing – original draft, Writing - review & editing, Supervision. **Guobiao Hu:** Software, Writing - review & editing.

Declaration of Competing Interest

The authors declare that they have no known competing financial interests or personal relationships that could have appeared to influence the work reported in this paper.

Acknowledgement

The author would like to acknowledge the financial support from the Natural Science Foundation of China (Grant No.12002152), Natural Science Foundation of Jiangsu Province (Grant No. BK20190379), China Postdoctoral Science Foundation Funded Project (Grant No.2020M681577) and a project funded by the Priority Academic Program Development of Jiangsu Higher Education Institutions.

References

[1] S. Priya, D.J. Inman, Energy Harvesting Technologies, Springer, 2009.
[2] Abdelkefi, Aeroelastic energy harvesting: a review, Int. J. Eng. Sci. 100 (2016) 112–135.
[3] M.K. Raj, M.C. Raj, Vortex induced vibration for aquatic clean energy, Appl. Mech. Mater. 110–116 (2012) 2117–2123.
[4] A.B. Rostami, M. Armandei, Renewable energy harvesting by vortex-induced motions: review and benchmarking of technologies, Renew. Sust. Energ. Rev. 70 (2017) 193–214.
[5] Z. Lai, S. Wang, L. Zhu, G. Zhang, J. Wang, K. Yang, D. Yurchenko, A hybrid piezo-dielectric wind energy harvester for high-performance vortex-induced vibration energy harvesting, Mech. Syst. Signal Pr. 150 (2021), 107212.
[6] S. Doare, Michelin, Piezoelectric coupling in energy-harvesting fluttering flexible plates: linear stability analysis and conversion efficiency, J. Fluid. Struct. 27 (2011) 1357–1375.
[7] K. Shoele, R. Mittal, Energy harvesting by flow-induced flutter in a simple model of an inverted piezoelectric flag, J. Fluid Mech. 790 (2016) 582–606.

[8] A. Barrero-Gil, G. Alonso, A. Sanz-Andres, Energy harvesting from transverse galloping, J. Sound Vib. 329 (14) (2010) 2873–2883.

[9] Z. Abdelkefi, M.R. Yan, Hajj, Modeling and nonlinear analysis of piezoelectric energy harvesting from transverse galloping, Smart Mater. Struct. 22 (2013), 025016.

[10] H.D. Akaydin, N. Elvin, Y. Andreopoulos, Wake of a cylinder: a paradigm for energy harvesting with piezoelectric materials, Exp. Fluids 49 (2010) 291–304.

[11] H.J. Jung, S.W. Lee, The experimental validation of a new energy harvesting system based on the wake galloping phenomenon, Smart Mater. Struct. 20 (2011), 055022.

[12] J. Wang, L. Geng, L. Din, H. Zhu, D. Yurchenko, The state-of-the-art review on energy harvesting from flow-induced vibrations, A. Energ. 267 (2020), 114902.

[13] J. Sirohi, R. Mahadik, Harvesting wind energy using a galloping piezoelectric beam, J. Vib. Acoust. 134 (2012), 011009.

[14] Jayant Sirohi, Rohan Mahadik, Piezoelectric wind energy harvester for low-power sensors, J. Intel. Mat. Syst. Str. 22 (18) (2011) 2215–2228.

[15] F. Ewere, G. Wang, B. Cain, Experimental investigation of galloping piezoelectric energy harvesters with square bluff bodies, Smart Mater. Struct. 23 (2014), 104012.

[16] Abdelkefi, M.R. Hajj, A.H. Nayfeh, Power harvesting from transverse galloping of square cylinder, Nonlinear Dynam. 70 (2) (2012) 1355–1363.

[17] Y. Yang, L. Zhao, L. Tang, Comparative study of tip cross-sections for efficient galloping energy harvesting, Appl Phys Lett 102 (2013), 064105.

[18] J. Wang, L. Tang, L. Zhao, Z. Zhang, Efficiency investigation on energy harvesting from airflows in HVAC system based on galloping of isosceles triangle sectioned bluff bodies, Energ. 172 (2019) 1066–1078.

[19] J. Wang, C. Zhang, S. Gu, K. Yang, H. Li, Y. Lai, D. Yurchenko, Enhancement of low-speed piezoelectric wind energy harvesting by bluff body shapes: Spindle-like and butterfly-like cross-sections, Aerosp. Sci. Technol. 103 (2020), 105898.

[20] W. Sun, F. Guo, J. Seok, Development of a novel vibro-wind galloping energy harvester with high power density incorporated with a nested bluff-body structure, Energ. Convers. Manage. 197 (2019), 111880.

[21] W. Sun, S. Jo, J. Seok, Development of the optimal bluff body for wind energy harvesting using the synergetic effect of coupled vortex induced vibration and galloping phenomena, Int. J. Mech. Sci. 156 (2019) 435–445.

[22] J. Wang, S. Sun, L. Tang, G. Hu, J. Liang, On the use of metasurface for Vortex-Induced vibration suppression or energy harvesting, Energ. Convers. Manage. 235 (2021), 113991.

[23] C. Zhang, G. Hu, D. Yurchenko, P. Lin, S. Gu, D. Song, H. Peng, J. Wang, Machine learning based prediction of piezoelectric energy harvesting from wake galloping, Mech. Syst. Signal Pr. 160 (2021), 107876.

[24] A.H. Bibo, M.F. Alhadidi, Daqaq, Exploiting a nonlinear restoring force to improve the performance of flow energy harvesters, J. Appl. Phys. 117 (2015), 045103.

[25] M.F. Bibo, Daqaq, An analytical framework for the design and comparative analysis of galloping energy harvesters under quasi-steady aerodynamics, Smart Mater. Struct. 24 (2015), 094006.

[26] A.H. Alhadidi, H. Abderrahmane, M.F. Daqaq, Exploiting stiffness nonlinearities to improve flow energy capture from the wake of a bluff body, Physica. D 337 (2016) 30–42.

[27] J. Wang, L. Geng, S. Zhou, Z. Zhang, Z. Lai, D. Yurchenko, Design, modeling and experiments of broadband tristable galloping piezoelectric energy harvester, Acta Mechanica Sinica 36 (3) (2020) 592–605.

[28] L. Zhao, Y. Yang, An impact-based broadband aeroelastic energy harvester for concurrent wind and base vibration energy harvesting, Appl. Energ. 212 (2018) 233–243.

[29] L. Lan, G. Tang, W. Hu, Qin, Dynamics and performance of a two degree-of-freedom galloping-based piezoelectric energy harvester, Smart Mater. Struct. 28 (2019), 045018.

[30] G. Hu, J. Wang, H. Qiao, L. Zhao, Z. Li, L. Tang, An experimental study of a two-degree-of-freedom galloping energy harvester, Int. J. Energy Res. 45 (2020) 3365–3374.

[31] L. Zhao, L. Tang, Y. Yang, Enhanced piezoelectric galloping energy harvesting using 2 degree-of-freedom cut-out cantilever with magnetic interaction, Jap. J. Appl. Phys. 53 (2014), 060302.

[32] K. Yang, J. Wang, D. Yurchenko, A double-beam piezo-magneto-elastic wind energy harvester for improving the galloping-based energy harvesting, Appl. Phys. Lett. 115 (2019), 193901.

[33] K. Yang, A. Abdelkefi, X. Li, Y. Mao, L. Dai, J. Wang, Stochastic analysis of a galloping-random wind energy harvesting performance on a buoy platform, Energy Conversion and Management 238 (2021), 114174.

[34] H. Abdelmoula, A. Abdelkefi, The potential of electrical impedance on the performance of galloping systems for energy harvesting and control applications, J. Sound Vib 370 (2016) 191–208.

[35] T. Tan, Z. Yan, Analytical solution and optimal design for galloping-based piezoelectric energy harvesters, Appl. Phys. Lett. 109 (2016), 253902.

[36] L. Zhao, L. Tang, J. Liang, Y. Yang, Synergy of wind energy harvesting and synchronized switch harvesting interface circuit, IEEE/ASME T. Mech. 22 (2) (2017) 1093–1103.

[37] L. Zhao, Y. Yang, Analytical solutions for galloping-based piezoelectric energy harvesters with various interfacing circuits, Smart Mater. Struct. 24 (2015), 075023.

[38] L. Zhao, Y. Yang, Comparison of four electrical interfacing circuits in wind energy harvesting, Sensor Actuat. A-Phys. 261 (2017) 117–129.

[39] L. Wang, T. Tan, Z. Yan, D. Li, B. Zhang, Z. Yan, Integration of tapered beam and four direct-current circuits for enhanced energy harvesting from transverse galloping, IEEE/ASME T. Mech. 24 (5) (2019) 2248–2260.

[40] Y. Yang, L. Tang, Equivalent circuit modeling of piezoelectric energy harvesters, J. Intel. Mat. Syst. Str. 20 (18) (2009) 2223–2235.

[41] J. Liang, W.-H. Liao, Impedance modeling and analysis for piezoelectric energy harvesting systems, IEEE/ASME T. Mech. 17 (6) (2012) 1145–1157.

[42] Lan, L. Tang, R.L. Harne, Comparative methods to assess harmonic response of nonlinear piezoelectric energy harvesters interfaced with AC and DC circuits, J. Sound Vib. 421 (2018) 61–78.

[43] Y. Liao, J. Liang, Unified modeling, analysis and comparison of piezoelectric vibration energy harvesters, Mech. Syst. Signal Pr. 123 (2019) 403–425.

[44] Y. Liao, J. Liang, Maximum power, optimal load, and impedance analysis of piezoelectric vibration energy harvesters, Smart Mater. Struct. 27 (2018), 075053.

[45] Lan, Y. Liao, G. Hu, T. Tang, Equivalent impedance and power analysis of monostable piezoelectric energy harvesters, J. Intel. Mat. Syst. Str. 31 (14) (2020) 1697–1715.

[46] L. Tang, L. Zhao, Y. Yang, E. Lefeuvre, Equivalent circuit representation and analysis of galloping-based wind energy harvesting, IEEE/ASME T. Mech. 20 (2) (2015) 834–844.

[47] C. Lan, L. Tang, W. Qin, Obtaining high-energy responses of nonlinear piezoelectric energy harvester by voltage impulse perturbations, Eur. Phys. J-Appl. Phys. 79 (2017) 20902.

[48] M.P. Païdoussis, S.J. Price, E. De Langre, Fluid-structure Interactions: Cross-flow-induced Instabilities, Cambridge University Press, 2010.

[49] Y. Liao, Analysis of power and efficiency of piezoelectric vibration energy harvesters through an impedance plot, Intel. Mat. Syst. Str. 30 (20) (2019) 3036–3055.

[50] K. Chen, J. Liang, Impedance analysis of piezoelectric energy harvesting system using synchronized charge extraction interface circuit, Proc. SPIE (2017) 101642Q.

[51] I.C. Lien, Y.C. Shu, Array of piezoelectric energy harvesting by the equivalent impedance approach, Smart Mater. Struct. 21 (2012), 082001.

[52] Y. Liao, H.A. Sodano, Piezoelectric damping of resistively shunted beams and optimal parameters for maximum damping, J. Vib. Acoust. 132 (2010), 041014.

[53] J. Liang, H.S.H. Chung, W.H. Liao, Dielectric loss against piezoelectric power harvesting, Smart Mater. Struct. 23 (2014), 092001.

[54] Q. Deng, Y. Liao, L. Zuo, P. Jones, System-level finite element analysis of piezoelectric energy harvesters with rectified interface circuits and experimental validation, Mech. Syst. Signal Pr. 151 (2021), 107440.